Solar Phys (2007) 243: 63–86
DOI 10.1007/s11207-007-0182-1

The X-Ray Telescope (XRT) for the *Hinode* Mission

L. Golub · E. DeLuca · G. Austin · J. Bookbinder · D. Caldwell · P. Cheimets · J. Cirtain · M. Cosmo · P. Reid · A. Sette · M. Weber · T. Sakao · R. Kano · K. Shibasaki · H. Hara · S. Tsuneta · K. Kumagai · T. Tamura · M. Shimojo · J. McCracken · J. Carpenter · H. Haight · R. Siler · E. Wright · J. Tucker · H. Rutledge · M. Barbera · G. Peres · S. Varisco

Received: 24 March 2006 / Accepted: 8 March 2007 /
Published online: 12 July 2007

Abstract The X-ray Telescope (XRT) of the *Hinode* mission provides an unprecedented combination of spatial and temporal resolution in solar coronal studies. The high sensitivity and broad dynamic range of XRT, coupled with the spacecraft's onboard memory capacity and the planned downlink capability will permit a broad range of coronal studies over an extended period of time, for targets ranging from quiet Sun to X-flares. This paper discusses in detail the design, calibration, and measured performance of the XRT instrument up to the focal plane. The CCD camera and data handling are discussed separately in a companion paper.

L. Golub (✉) · E. DeLuca · G. Austin · J. Bookbinder · D. Caldwell · P. Cheimets · J. Cirtain · M. Cosmo · P. Reid · A. Sette · M. Weber
Harvard-Smithsonian Center for Astrophysics, 60 Garden Street, Cambridge, MA 02138, USA
e-mail: lgolub@cfa.harvard.edu

T. Sakao
Institute of Space and Astronautical Science, Japan Aerospace Exploration Agency, 3-1-1 Yoshinodai, Sagamihara, Kanagawa 229-8510, Japan

R. Kano · H. Hara · S. Tsuneta · K. Kumagai · T. Tamura
National Astronomical Observatory, Mitaka, Tokyo 181-8588, Japan

K. Shibasaki · M. Shimojo
Nobeyama Solar Radio Observatory, National Astronomical Observatory, Minamimaki, Minamisaku, Nagano 384-1305, Japan

J. McCracken · J. Carpenter · H. Haight · R. Siler · E. Wright · J. Tucker · H. Rutledge
NASA/Marshall Space Flight Center, Huntsville, AL 35812, USA

M. Barbera · G. Peres · S. Varisco
Osservatorio Astronomico di Palermo "G.S. Vaiana", Piazza del Parlamento 1, 90134 Palermo, Italy

1. Introduction to XRT and *Hinode*

The solar outer atmosphere presents a unique set of problems for the observer: The temperature varies from 5800 to more than 10^7 K, with a consequent range in primary emission wavelengths; the target has a large angular size while much of the relevant physics takes place on very small spatial scales; the aspect of most interest, the variability of the atmosphere, is due to the presence of strong and intermittent magnetic fields rooted in the photosphere. The **B** field traverses a broad temperature regime from the visible surface to the corona. The wavelengths that need to be observed cover a comparable range, from visible to X-ray, and the spatial scales that need to be resolved range from a fraction of an arcsec at the surface to $>10^5$ km in the corona; the time scales that need to be studied range from microseconds to years (Golub, 2003). The combination of instruments chosen for the *Hinode* mission has been selected with these considerations in mind.

2. Brief Science Overview

Because the solar outer atmosphere is at a temperature of several million kelvins (MK) its primary emission is in the soft X-ray spectral range. X-ray images display the spatial distribution of this high-temperature plasma, and diagnostics are available to determine the distribution as a function of temperature of the coronal material. The X-ray Telescope (XRT) provides an unprecedented combination of spatial, spectral, and temporal coverage, which will allow a broad range of scientific investigations to be carried out, as listed in Table 1. In addition to the inherent capabilities of the XRT, the spectral data provided by EIS and spectroheliograms and the **B** measurements from SOT/FPP will greatly extend our analytic capability in studies of the structure and dynamics of the solar atmosphere.

The XRT provides several "firsts" in capability in comparison with previous X-ray imagers. Some of these are summarized in the following, and further details are presented in Deluca *et al*. (2005):

Table 1 Scientific objectives of the XRT.

Objective	Representative questions
1. Coronal mass ejections	How are they triggered? What is relation to **B** structure? What is relation between large-scale instabilities and dynamics of fine structure?
2. Coronal heating	How do coronal structures brighten? Are there waves, and do they correlate with brightness? Do loop – loop interactions cause significant heating?
3. Reconnection and jets	Where and how does reconnection occur in the corona? What is its relation to B?
4. Flare energetics	Same as Item 1 above
5. Photosphere – corona coupling	Can a direct connection between coronal and photospheric events be established? How is energy transferred to the corona? What determines coronal transverse fine structure?

– Unprecedented combination of spatial resolution, field of view, and image cadence.
– Broadest temperature coverage of any coronal imager to date.
– High data rate for observing rapid changes in topology and temperature structure.
– Extremely large dynamic range to detect corona from coronal holes to X-flares.
– Flare buffer, onboard storage, and high downlink rate.

2.1. Instrument Flowdown Requirements

The scientific objectives that have been specified for the XRT lead to a set of flowdown requirements, as shown in Table 2. These are the minimum performance requirements needed to meet the objectives; in most cases the as-built XRT exceeds these requirements, as will be discussed in the following.

These requirements lead to the choice of a grazing-incidence (GI) X-ray telescope, with a design chosen to meet the specific requirements. We note that the XRT design provides image quality in the central portion of the field that is as good as manufacturing tolerances allow, so that no further improvement in image quality could be considered. The design and fabrication of the XRT are discussed in detail in Section 3.1.

2.1.1. XRT Temperature Sensitivity

Requirements 3 and 4 in Table 2 may be singled out as involving more of the telescope design elements simultaneously than any of the other requirements. There are a number

Table 2 Instrument flowdown requirements.

Requirement	Definition	Value
1. Exposure time	Shutter-open time	4 ms – 10 s
2. Cadence	Time between exposures	2 s (reduced FOV)
3. T range	Limits of temperature coverage	$6.1 < \log T < 7.5$
4. T resolution	Ability to discriminate temperatures	$\log T = 0.2$
5. X-ray optical resolution	Diameter of 50% enclosed energy	2 arcsec PRF
6. Field of view	Angular coverage of telescope	>30 arcmin
7. WL rejection	Reduction of solar visible light at focal plane	$>10^{11}$
8. Data rate	Maximum bit transfer rate out of XRT	2.4 Mb/s
9. Data volume	Maximum volume per memory fill cycle	60 MB/orbit
10. Coordination X-ray/WL (spatial)	Coalign X-ray and WL	One XRT pixel
11. Coordination XRT/SOT (spatial)	Coalign XRT to SOT	One XRT pixel
12. Coordination XRT/EIS (spatial)	Coalign XRT to EIS	One XRT pixel

of factors involved in determining the temperature range of a GI telescope, and additional factors determine the temperature sensitivity. Design elements include the reflectance of the telescope as a function of incoming photon energy E; the transmission of the entrance aperture prefilters as $f(E)$; the transmission of the focal plane analysis filters as $f(E)$; and the response of the focal plane detector as $f(E)$. We see that each of the major subsystems of the XRT contributes to this requirement. In the following sections we discuss the major subassemblies of the XRT separately. The overall temperature response and temperature discrimination of the XRT will be discussed subsequently.

3. Major Subsystems

The components of the XRT are shown schematically in Figure 1. The XRT is, in principle, a simple instrument: a grazing-incidence optic focuses solar soft X-rays onto a CCD array. Separation between the two is maintained by a stiff, lightweight, low-expansion carbon-fiber-reinforced polymer (CFRP) tube. The front of the telescope is covered with thin filters to reduce the visible light entering the telescope, and additional filters are positioned in the optical path ahead of the CCD camera, along with a shutter assembly. A focus mechanism allows the camera to be moved ± 1 mm along the optical axis. A visible light optic is included in the center of the X-ray mirror to provide aspect information for the XRT and for the *Hinode* mission as a whole. The telescope (*i.e.*, the mirror) is shown schematically in Figure 2. Its design is discussed in detail in Section 3.1.

3.1. Mirror

Grazing-incidence optics used for soft X-ray imaging generally require a minimum of two surfaces to meet the Abbé sine condition that the magnification be constant over the full aperture of the telescope. Wolter used a paraboloid – hyperboloid design, and the more complex Wolter – Schwarzschild design improves image quality slightly by exactly satisfying the condition. Werner (1977) recognized that for a wide-field instrument the field-averaged point spread function (PSF) is a better figure of merit to use, and modern computer polishing methods permit the implementation of designs using high-order polynomial surfaces that deviate from the more standard conic sections. These designs generally trade on-axis image quality for off-axis improvements. This is acceptable because perfect surfaces cannot

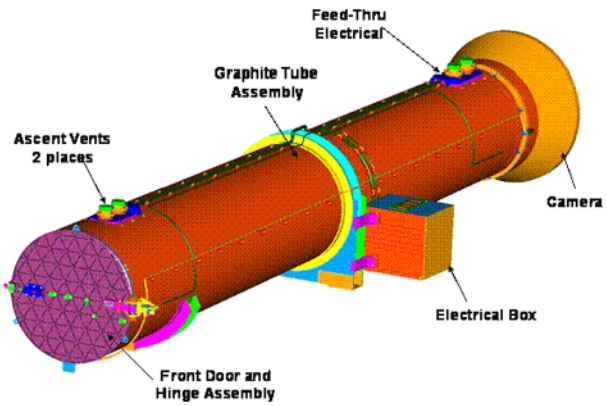

Figure 1 The major components of the XRT; the optics are located inside the entrance aperture door.

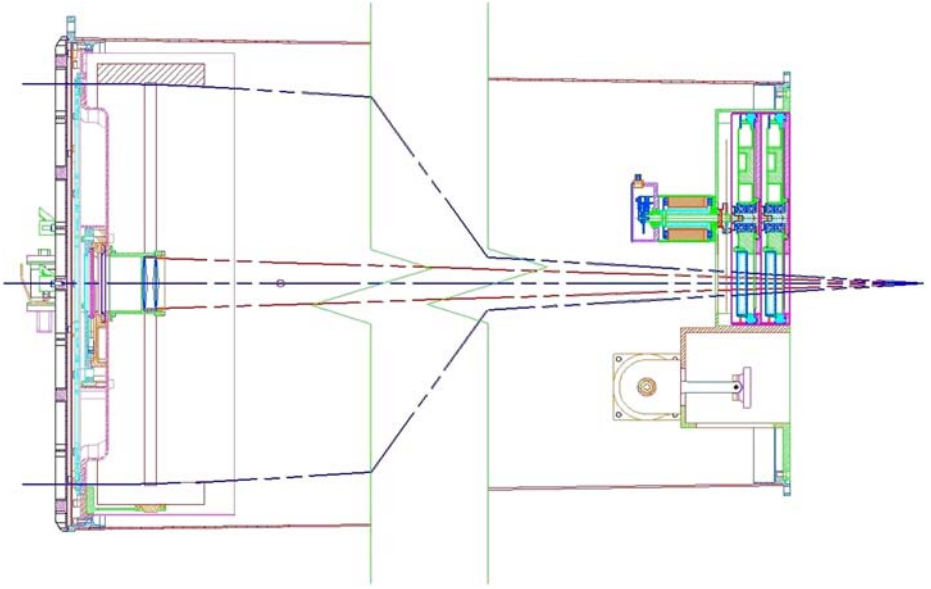

Figure 2 A schematic diagram of the grazing-incidence XRT including the entrance filter assembly and the centrally located visible light telescope. The GI telescope is shown in section (cross-hatched). The shutter, filter wheel, and focus mechanism (US portion) are shown at right. Note that the central part of the CFRP metering tube has been omitted and that the camera is not shown.

be manufactured, so that there is relatively little loss on axis, whereas the off-axis gain can be considerable. In addition, the detector can be positioned slightly out of focus and thereby achieve a better PSF at finite field angle, at the cost of on-axis performance; this was done, *e.g.*, for the *Yohkoh* SXT (Nariai, 1987, 1988; Tsuneta *et al.*, 1991).

The XRT uses a generalized asphere for each mirror element and also has a focus mechanism that allows images to be obtained at the best on-axis (Gaussian) focus and at a range of defocus positions. The variation of image quality versus field angle can be varied by changing the location of the focal plane, as shown in Figure 3.

3.1.1. Goodrich

3.1.1.1. As-built The telescope as delivered to SAO met all of the design requirements except for knowledge of the focal length, as shown in Table 3. The stated encircled energy diameter requirement was for the optical design itself, and the delivered performance matches the requirement for 2 arcsec imaging.

3.1.1.2. Performance Predictions Measurements of the as-built telescope at Goodrich were used to calculate the expected optical performance of the XRT. Figure 3 shows the predicted as-built RMS point response function (PRF) versus field angle at different field angles. Comparison with the measured PRF will be presented in Section 4 of this paper.

The size and shape of the PRF are functions of position in the field and of focal plane location along the optical axis. This is illustrated by Figure 4 (top), which shows the PRF at several off-axis locations for a focal plane located 200 μm ahead of the best Gaussian focus. The corresponding encircled energy plots are shown in Figure 4 (bottom). These plots are again predictions based on the measurements of the as-built XRT.

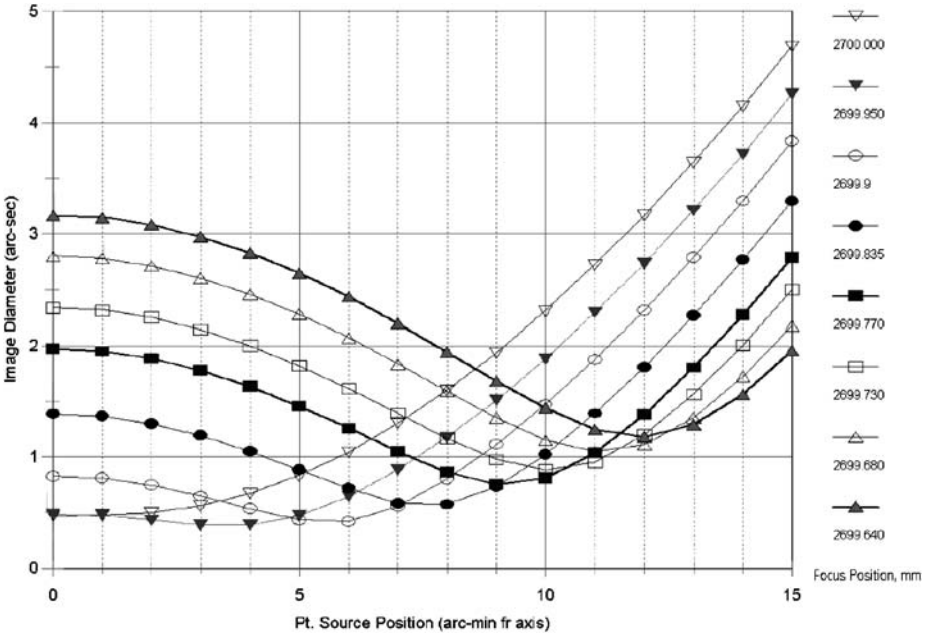

Figure 3 The predicted point response function of the XRT as a function of focal plane location, based on Goodrich measurements of the mirror surface shape.

Table 3 As-built XRT performance parameters.

Parameter	Requirement	As-built
Optical design	Single mirror pair	Generalized asphere
Wavelength range	6 – 60 Å	Bare zerodur
Entrance diameter	341.7 ± 0.1 mm	341.7 mm
Focal length	2708 ± 2 mm	2707.5 mm
Focus knowledge	± 0.050 mm	± 1.4 mm
Field of view	35 arcmin	Optimized over 15 arcmin
Encircled energy	68% at 0.5 keV	68% at 0.56 keV
(diameter)	1.57 arcsec	2.3 arcsec
Effective area	1.0 cm^2	1.9 cm^2

The focal length of the XRT (and of GI telescopes in general) is dependent on field angle because of focal plane curvature. The predicted values at field angles of 0, 5, 10, and 15 arminutes are 2707.5, 2707.0, 2706.8, and 2707.2 mm, respectively. The spot centroid for these off-axis point source images is located $\approx$0.78553 mm/arcmin from the on-axis field center; this quantity is the plate scale.

The measured performance of the XRT will be discussed in Section 4 where we present results of the extensive calibration and testing that were carried out at the X-Ray Calibration Facility (XRCF) of the Marshall Space Flight Center.

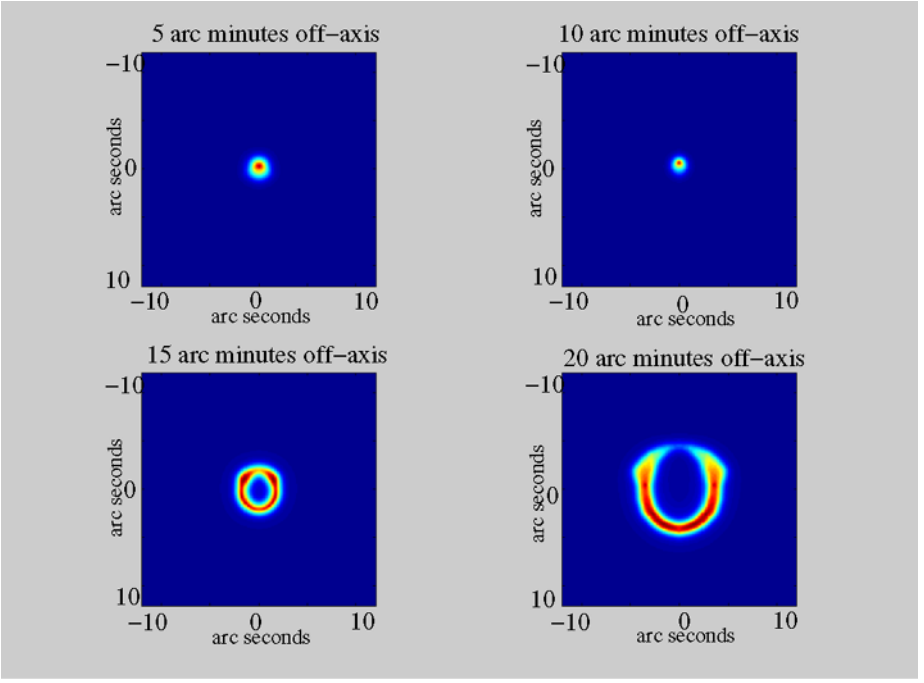

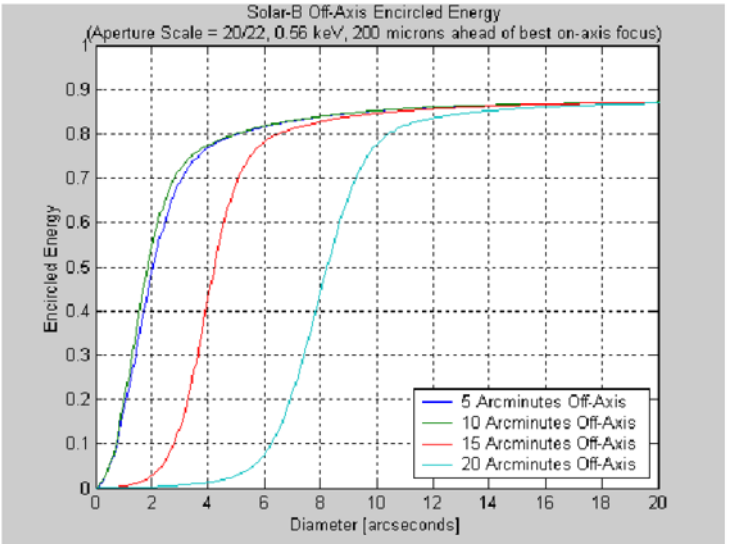

Figure 4 The predicted PRF of the XRT for off-axis angles at a focus position 200 μm forward of best focus. The top image shows the focal spot and bottom figure shows the corresponding encircled energy curves (Courtesy Goodrich – Danbury).

3.2. Filters

The XRT utilizes both entrance aperture prefilters and focal plane analysis filters; these are discussed in the next two sections. We note here that the visible-light-blocking requirement for the XRT is 10^{-12}, which translates into a requirement for the prefilter and analysis filters of 10^{-6} each. This requirement determines the minimum acceptable thickness for each filter. It also drives the mechanical design when launch vibration and acoustic loads are taken into account, since the filters must remain light-tight into orbit.

3.3. Prefilters

Thin prefilters cover the narrow annular entrance aperture of the XRT. These prefilters serve two main purposes: (1) to reduce the visible light entering the instrument and (2) to reduce the heat load in the instrument.

Taking into account the amount of visible light attenuation needed to allow soft X-ray detection at the focal plane CCD, and also taking into account the available methods for reducing visible light entering the telescope, we find that Requirement 2 is automatically met when Requirement 1 is met. We will therefore discuss only the first item.

Ideally, the prefilter will reduce the visible light as much as possible and will reduce the X-ray throughput as little as possible. Experience has shown that the material best suited for this purpose is aluminum and we will treat only this choice. However, there are several additional factors to consider: Aluminum oxidizes from the moment of manufacture until launch. The rate is strongly affected by humidity, so that handling in dry nitrogen is important. Additionally, Al filters exposed to full Sun in vacuum will become hot. Thermal conduction along the filter to the frame that supports it will cool the filter, and the path length is a major factor in determining the temperature on orbit. Finally, to strengthen the filter against launch loads, the aluminum can be mounted on a mesh, on a thin organic film such as polyimide, or on both.

The severity of the vibration and acoustic loads for the *Hinode* launch, combined with the availability of thin, strong, highly transmissive polyimide from the Luxel Corp. determined the choice of substrate thickness. The amount of Al need to provide the required visible light blocking determined the Al thickness. The XRT entrance filters consist of 1200 Å Al and 2500 Å of polyimide, with an estimated 100 Å of Al_2O_3. A photo of one entrance filter is provided in Figure 5.

3.4. Focal Plane Analysis Filters

The analysis filters serve two purposes: (1) to reduce the visible light reaching the focal plane and (2) to provide varying X-ray passbands for plasma diagnostics. The analysis filters are held in two filter wheels, operated in series and located in front of the CCD camera, near the focal plane (Figure 6).

The analysis filters, differing in thickness by nearly a factor of 10^4, greatly extend the dynamic range of the XRT, For faint targets, which also tend to have relatively low temperatures, the thinner filters are used. For flare observations the thickest filters are used. In addition, there is a focal plane filter used with the visible light telescope, which is operated separately from the X-ray channel. This glass filter may also be inserted during X-ray observations in the rare event that the flare intensity exceeds the instrument saturation level.

Inserting the analysis filters into the optical path alters the throughput of the telescope as a function of wavelength. Combined with software that calculates the spectral emissivity of

Figure 5 One of the six annular aluminized polyimide entrance filters of the XRT.

Figure 6 One of the two XRT filter wheels, each of which holds five filters and has one open position.

the coronal plasma as a function of its temperature (Smith *et al.*, 2001), we may calculate the response of the XRT for the various analysis filters. This calculation is shown in Figure 7, in which the throughput of the telescope is shown for an assumed source with constant emission measure (amount of material) as a function of temperature of 1×10^{30} cm^{-5} over the entire XRT sensitivity range. The units are erg cm^{-2} s^{-1} at the focal plane, so that the CCD response is not included. These curves represent the basic first step in the quantitative analy-

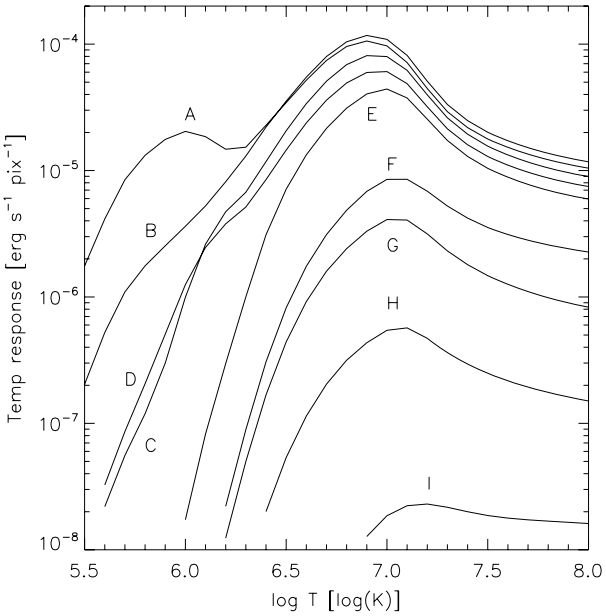

Figure 7 The total XRT temperature response, for all of the X-ray focal-plane filters. Each curve plots the combination of the total instrument response (as a function of wavelength) with a coronal plasma emission model (ATOMDB/APEC) for a columnar emission measure of 10^{30} cm^{-5}. The labels indicate which filter is in the path, as follows: A = Al-mesh, B = Al-poly, C = C-poly, D = Ti-poly, E = Be-thin, F = Be-med, G = Al-med, H = Al-thick, and I = Be-thick.

Table 4 Physical characteristics of the XRT focal plane analysis filters.

Filter ID	Material	Thickness (Å)	Filter support	Thickness (Å)	Oxide	Thickness (total, Å)
Al-mesh	Al	1600	–	82%	Al_2O_3	150
Al-poly	Al	1250	Polyimide	2500	Al_2O_3	100
C-poly	C	6000	Polyimide	2500	N/A	N/A
Ti-poly	Ti	3000	Polyimide	2300	TiO_2	100
Be-thin	Be	9E4	N/A	N/A	BeO	150
Al-med	Al	1.25E5	N/A	N/A	Al_2O_3	150
Be-med	Be	3.0E5	N/A	N/A	BeO	150
Al-thick	Al	2.5E5	N/A	N/A	Al_2O_3	150
Be-thick	Be	3.0E6	N/A	N/A	BeO	150

sis of XRT images; a typical next step might be the type of analysis described in Section 5.4 to determine the distribution of the EM in a target region of interest.

3.4.1. Filter Specification

A summary of the nominal physical properties of the focal plane analysis filters is provided in Table 4. The measured values for the component thicknesses are discussed in the next section.

3.4.2. Palermo Testing

Several of the flight focal plane filters for the XRT were tested at the X-Ray Astronomy Calibration and Testing (XACT) facility of INAF – Osservatorio Astronomica di Palermo.

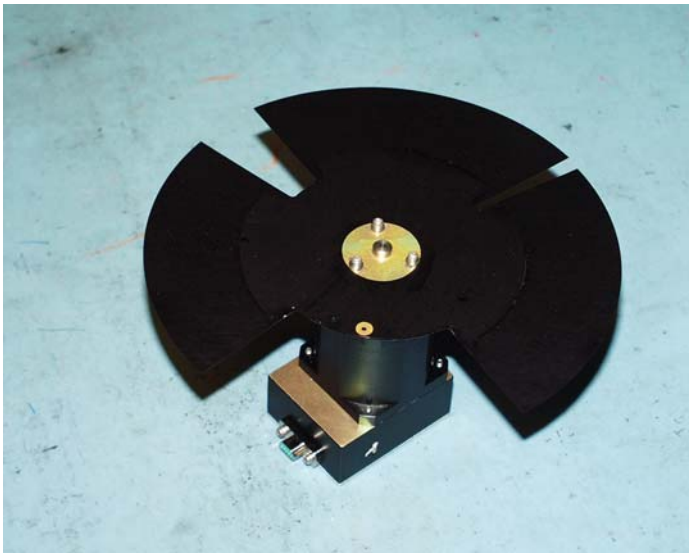

Figure 8 The XRT shutter is a thin rotating blade with two narrow slits for 1 and 8 ms exposures, plus a slot for exposure times ≥44 ms.

The goal of these calibrations was to determine the spatial uniformity of the filters and the transmission properties (Barbera *et al.*, 2004). Of the nine filters tested, seven are installed in the XRT, since several were damaged in shipping and needed to be replaced. The results show that the spatial uniformity is 2% or better for the metal on polyimide filters and better than 3.3% for the single metal filters. The transmission tests showed that the results were within 5 – 10% of the predicted values.

After launch of the XRT the witness samples for the flight filters (entrance and focal plane) will be measured for transmission at the XACT. This will provide the final transmission calibrations.

3.4.3. XRCF Testing

The transmissions of the focal plane filters listed in Table 4 were also measured during the end-to-end test at the XRCF. The measured transmissions are within 5 – 20% of the predicted values for all of the exposures with a high photon flux. Table 6 shows the sources that we had available to us for these tests, and Table 7 shows the comparison of measured and predicted transmissions.

3.5. Shutter

The focal plane shutter used in the XRT is a modified version of the TRACE shutter (Figure 8). It can be operated in two modes: a continuous sweep at fixed rotation speed or a start – stop mode in which the large opening is brought into the path and kept there for the desired length of time. The narrow openings may be employed in a multiple-pass mode, so that a large set of exposure times can be used. The set of exposure times chosen for initial operations is given in Table 5.

Table 5 Initial table of available XRT exposure values.

ID#	τ_{exp} (s)	ID#	τ_{exp} (s)
0	0.001	18	0.71
1	0.002	19	1.00
2	0.003	20	1.41
3	0.004	21	2.00
4	0.005	22	2.83
5	0.008	23	4.00
6	0.012	24	5.66
7	0.016	25	8.00
8	0.024	26	11.3
9	0.032	27	16.0
10	0.044	28	22.6
11	0.063	29	32.0
12	0.086	30	45.2
13	0.125	31	64.0
14	0.177	32	64.0
15	0.250	33	64.0
16	0.354	34	64.0
17	0.500	35	64.0

3.6. WL Telescope

The XRT includes a visible light imager coaxial and confocal with the X-ray telescope. It is a simple achromat designed to image the Sun in the 400 – 500 nm band with 2 arcsec spatial resolution. The lens materials, fused silica and SF16, are chosen for their insensitivity to radiation darkening and are used to correct axial color between 405 and 495 nm; the design also corrects for spherical aberration at 430 nm.

The nominal focal length of the doublet is 2705 mm, and the aperture is 50 mm, giving an f-number of f/54. The optic is mounted in a manner that permits adjustment along the optical axis so that the visible light focal plane is positioned coincident with the as-built X-ray focal plane, to within the depth of focus of the XRT. The WL depth of focus is substantially larger than the XRTs.

The WL Telescope is fitted with an entrance aperture filter manufactured by the Andover Corporation and having a passband centered on the G band at 430.7 nm with a FWHM of 18.9 nm. A similar filter is placed in one of the focal plane filter wheels, with a tested central wavelength of 430.3 nm and FWHM of 17.7 nm. The peak transmissions of the filters are 49.3% and 29.6%, respectively, including a built-in neutral density coating on the focal plane filter for off-band rejection. The additional neutral density filter, of ND = 1.3, was selected to provide a nominal exposure time of 1/100 s. The correct ND value was chosen by calibrating the WL Telescope at Williams College by using their 0.6 m solar telescope and obtaining images at varying elevations, so that an extrapolation to zero air mass could be obtained.

3.7. Visible Light Imager and X-Ray Telescope Confocality

The XRT and visible light imager (VLI) share a CCD camera and a focus mechanism that has a range of motion of ± 1 mm. Therefore, to achieve the required optical performance,

it is necessary that their respective best on-axis focus positions both lie within the range of the focus mechanism. To reasonably minimize cadences and the frequency of mechanism motions, it is desirable that the best on-axis focus position for the VLI lie within 250 μm of that for the XRT. This value is substantially smaller than the depth of focus of the VLI, so that refocusing in switching from XRT to VLI would not be needed.

Observations were taken of a visible light penray lamp at the same distance along the facility axis as the X-ray source. Measurements were taken across the range of focus mechanism positions, with the VLI shutter in both the open and closed states. At this point in the end-to-end test, the telescope configuration included the finite source spacer, but not the entrance filters. Therefore, images taken with the VLI shutter open registered light traversing both the XRT and VLI optic. Images taken with the VLI shutter closed registered light traversing the XRT optic. To isolate an image focused solely by the VLI optic, each closed image is subtracted from its corresponding open image. This subtraction also compensates for dark current in the image.

The images of the visible light source were fitted with a 2D Gaussian model, which is valid for focus positions near best focus. The RSS Gaussian widths are then plotted as a function of focus position (Figure 9). The best on-axis focus position is defined to be where the RSS Gaussian width is a minimum. However, analysis indicates that, over the range of motions available in the XRT, the data are well fit with a horizontal straight line. This result corresponds to an instrument that has a broad depth of focus, in which case all (on-axis) focus positions produce images with equivalent focus.

The VLI data are consistent with the prediction that the VLI would have a depth of focus (2.2 mm) broader than the range of motion of the focus mechanism (1.0 mm). (Note that the size of the spot in Figure 9 includes the finite size of the lamp used to produce the WL

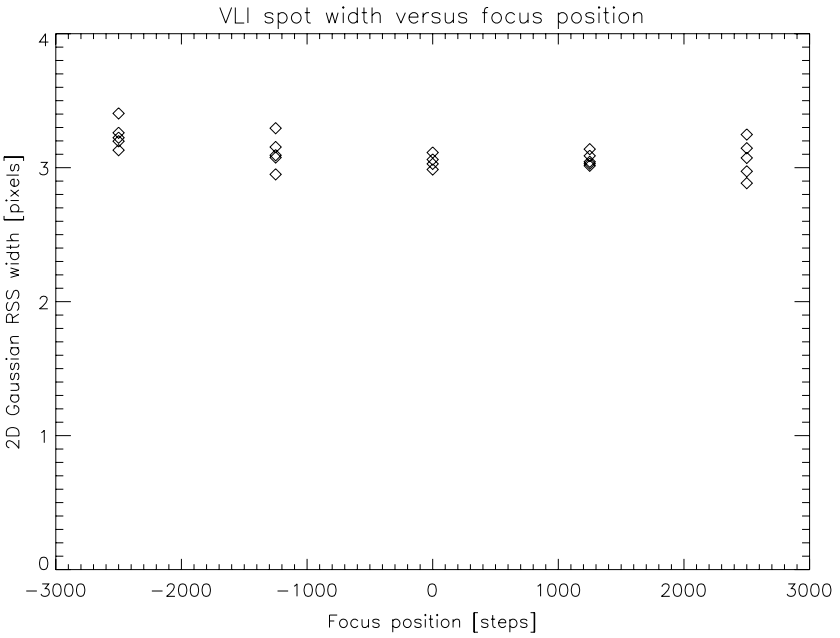

Figure 9 The spot size of a visible light source imaged through the visible light imager (VLI) as a function of distance along the optical axis of the XRT.

image at the XRCF.) Therefore, any VLI focus position within 250 μm (≈500 steps in the diagram) of the XRT best-focus position will give acceptable focus of the VLI.

3.8. Visible Light Imager and X-Ray Telescope Coalignment

The visible light source was placed adjacent to the X-ray source at the same horizontal distance (530.6 m) from the front of the XRT instrument along the facility axis, but laterally offset by 14.1 cm.

For the X-ray measurements, the Cu – L source was used. Normal images were taken at the best-focus position, and the XRO peak flux centroids were located to ±0.5 arcsec, *i.e.*, one pixel on the CCD. For the VLI measurements, normal images were taken at the nominal 430.5 nm focus position, and the VL peak flux centroids were also located to ±0.5 arcsec.

The measured offset between the XRT and VLI centroids was corrected for the physical offset of the sources and an estimate of the error in the measure of the offest. The VLI and XRT axes net alignment offset is 17.0 ± 5.0 arcsec, with the uncertainty dominated by the $\approx 1/4''$ uncertainty in the location of the visible light source. This alignment accuracy is well within the required coalignment tolerance of one arcmin. The tighter requirement on *knowledge* of the coalignment is determined after launch during the commissioning phase of the satellite.

4. XRT Mirror Imaging Performance

Two major test sequences of the XRT were carried out at NASAs XRCF. In the first (mirror calibration test), the imaging properties such as point response function, effective area as a function of wavelength, and off-axis response of the XRT were determined. The XRT was then returned to the XRCF after assembly into flight configuration, specifically to establish the focal length via an end-to-end test. Image performance data from both the mirror calibation and end-to-end test are presented in this section. The total telescope throughput is discussed in the following section. Details of the CCD camera calibration are discussed in the companion XRT camera paper (Kano *et al.*, 2007).

4.1. Test Plan

The XRCF consists of an X-ray source located at one end of a 518 m vacuum pipe, with a large vacuum chamber at the other end of the pipe to hold the test article and associated test equipment. Our tests used an electron impact point source, in which an electron beam is focused onto a target, at a voltage chosen to excite a characteristic line; typically K-α or L-α lines are chosen, for strength and spectral purity. A thin metallic filter, usually of the same material as the target, is then placed in the path to filter out unwanted X-ray energies while permitting the characteristic X-rays to pass. The primary lines used in this test are listed in Table 6.

The mirror calibration tests carried out were as follows:

Focus Determination: The mirror is aligned with the source – detector line. A scan through the focus range was performed and 2D Gaussian curve fits were applied to images. The best on-axis focus (BF) was located by the minimum in the polynomial fit of the RSS sigma width values for the FWHM. The focus position that provides the best average imaging across the field of view (FOV) is called the FOV Optimized Focus (OF), defined as the position where the on-axis FWHM is equal to 2″. This yields the largest extent of field angles meeting the resolution requirement.

Table 6 Available X-ray lines for the XRT calibration at the XRCF.

Line	Energy (keV)	Wavelength (Å)
C – K	0.277	44.7
O – K	0.525	23.6
Cu – L	0.933	13.3
Al – K	1.49	8.3
Mo – L	2.29	5.4

On-Axis PSF and Encircled Energy: Characterization of the performance of the XRT mirror was performed after completion of the optical axis alignment of the mirror to the X-ray beam. Data were collected using the Cu – L source from both the CCD and proportional counters. The combination of these data was used to find the PSF and encircled energy.

On-Axis Effective Area: A flow proportional counter (FPC) with a wide pinhole aperture was used to alternately measure the photon count rate through the effective area of the X-ray optic and through the unobstructed visible light aperture along the same optical axis. The ratio of the on-axis effective area to the calibrated pinhole aperture area is equal to the ratio of the photon count rate through the respective areas. Independent measurements of the source flux rate provided normalization against time variations. Proportional counter data were taken with the five different energy sources (Table 6).

Off-Axis PSF and Encircled Energy: This test was performed with the Cu – L (0.933 keV) source, using an off-axis configuration of 15.6 arcmin. The X-ray beam center was measured with an FPC and an array of calibrated pinhole apertures from 20 μm to 20 mm. These data were used to characterize both the off-axis PSF and encircled energy performance of the XRT optic.

Off-Axis Effective Area: The XRT off-axis effective area was measured at an angular displacement of 15.6 arcmin (immediately subsequent to the off-axis PSF measurements). The 20 mm pinhole aperture and an FPC detector were used to sample the beam center for both the Cu – L (0.933 keV) and O – K (0.525 keV) X-ray sources, in conjunction with measurements through the VLI. In other respects, the test procedure was identical to that described for the on-axis effective area measurements.

Wings of the PSF: To determine the contribution of the wings of the PSF, 89 normal and dark images were collected at best on-axis focus. A subset of these images were calibrated and summed. Fluxes within annuli approximately 3 CCD pixels thick were summed with the midpoint radius of each annulus expanding toward the edge of the CCD in discrete steps of 3 CCD pixels.

Thermal Response of the Telescope: Images were collected at three different chamber temperature configurations: at 15°C, at 22°C, and with a 1°C temperature gradient around the mirror circumference. Analysis of any observed variation in the PSF FWHM was made.

4.2. Best On-Axis Focus PSF

The BF was found as described in the previous section. During the mirror calibration tests data involving subpixel motions were collected to help determine the azimuthal location of best focus. In this procedure, images were taken after the CCD position was shifted 7 μm ($\approx 1/2$ pixel) in both the $\hat{z}$ and the $\hat{y}$ directions. An estimate of the PSF was derived from these data via an interpolation method (Figure 10), after which corrections for the finite

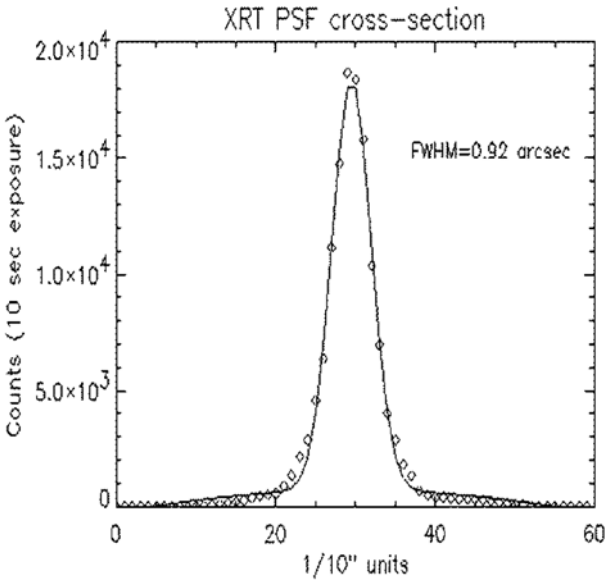

Figure 10 The PRF of the XRT before correction for the finite source distance during XRCF testing and for the deformations from gravity. The FWHM is less than one XRT CCD pixel.

source distance and the effect of gravity were applied to derive the PSF as it will appear in flight configuration (Figure 11).

After the PSF is constructed, annuli of successively increasing inner radii were formed, with the peak of the PSF taken as the origin of all of the annuli. The fluxes contained within these 2-pixel-thick annuli were summed and plotted as a function of diameter of the annuli. The resulting plot is shown as one of the curves in Figure 12. This plot shows that the mirror meets the NASA requirement that 50% of the encircled energy be contained within a diameter of 27 μm (2 arcsec).

The PSF was also measured via a series of pinholes positioned on axis at the plane of best focus, with a proportional counter located behind the pinholes. These measurements confirmed the size and shape of the inner core of the PRF and were also used to measure the large-angle wings of the PRF; those results are presented in Section 4.3.

The PSF as measured contains two contributions that are not present on orbit: The XRCF source is of necessity located at a finite distance from the telescope, and the optic is distorted from the effect of gravity. We have modeled both of these effects and corrected the measured PSF, with the result shown in Figure 11.

4.2.1. Mirror Contribution

The experimentally determined encircled energy function of the XRT is shown in Figure 12, which compares the prediction with two measurements, one using a CCD and one using a nested sequence of pinholes. The only discrepant data point is that using the large (50 μm) pinhole; this is being investigated. The CCD contribution to the instrument PRF is discussed in the companion paper in this volume.

4.2.2. Performance across the FOV

Images taken at Cu – L (0.933 keV) across the field of view of the XRT are used to determine the PSF when the camera is positioned at the plane of best focus. The results are summarized

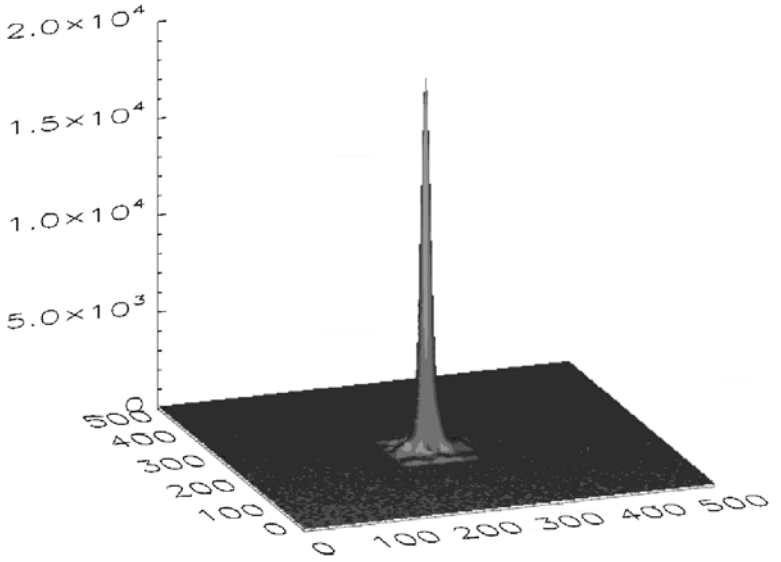

Figure 11 The PRF of the XRT corrected for the finite source distance during XRCF testing and for the deformations from gravity. The FWHM is ≈0.8 arcsec, less than one XRT CCD pixel.

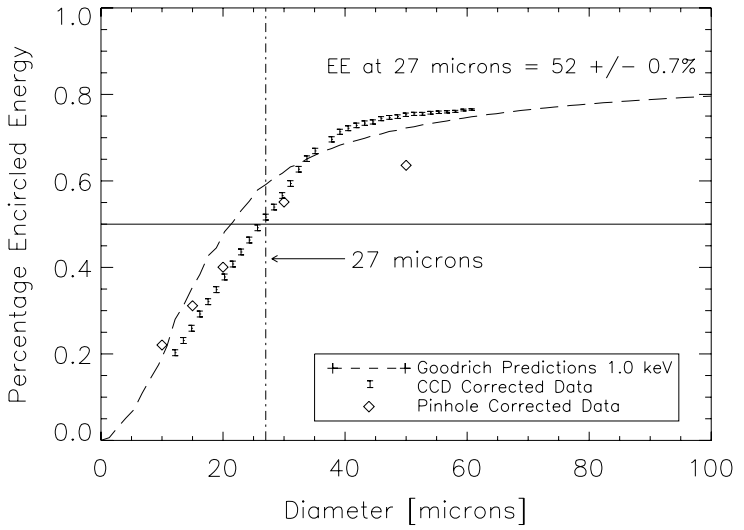

Figure 12 The predicted vs. measured encircled energy function of the XRT for the on-axis Gaussian focus position. The dashed line is the Goodrich prediction and the diamonds and brackets indicate the experimental values.

and compared to a curve showing the variation in RMS spot size versus field angle obtained using a ray trace program that takes the measured telescope surface figure. Comparison of the spot size data obtained at the XRCF after finding the location of best focus to the predictions is shown (Figure 13). We find excellent agreement between the predicted performance and the measured values.

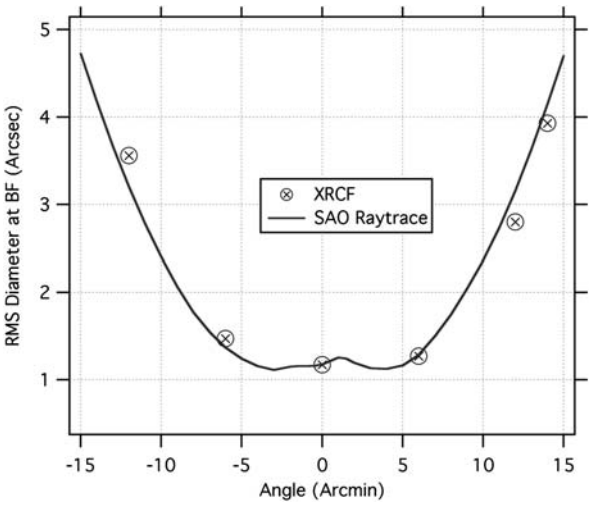

Figure 13 The measured vs. predicted off-axis spot size in test configuration (*i.e.*, without the 1G and finite source distance corrections).

4.3. Wings and Scattering

The wing response is defined as the ratio of the off-axis flux to the on-axis flux for a point source. The off-axis angle must also be specified and for the XRT the requirement was specified for an annular ring of width 1 arcsec located at a radius of 60 arcsec. The wing response was measured at the XRCF for the full range of angles from 0 to slightly more than 60 arcsec by using the CCD images for the bright inner portion of the PSF and the pinhole measurements for the faint outer portion. Ten long-exposure CCD images were averaged for the core determination and the result was spliced onto the pinhole data in their overlap region. The wing response of the XRT PSF (Figure 14) was sampled with an FPC by using 100 and 300 μm calibrated pinhole apertures, at a range of positions between 0 and 1000 μm from the core center. A 2D Lorentzian model was fit to this dataset. The PSF core was sampled with an FPC by using a 10 μm pinhole, in a 7×7 array of positions within 22 μm of the core center. A 2D Gaussian model was fit to this latter dataset. The Gaussian core and Lorentzian wing models were matched at 13 μm, and together they were normalized to the core peak value. The measurements shows that the scattering is $<10^{-5}$ at 1 arcmin off-axis, at an energy of 0.93 keV.

5. Throughput

5.1. Mirror Effective Area

The effective area of the XRT depends upon the geometric area and the reflectance of the mirror surfaces. The latter quantity is wavelength dependent and enters twice because the XRT is a two-bounce telescope. The predicted effective area agrees well with the measured area, as shown in Figure 15. The effective area at an off-axis angle of 15.6 arcmin was also measured, as shown in the figure; the lower reflectance indicates the degree of vignetting at this angle. The overall XRT response also includes the entrance filter and the focal plane analysis filter transmissions and the CCD efficiency.

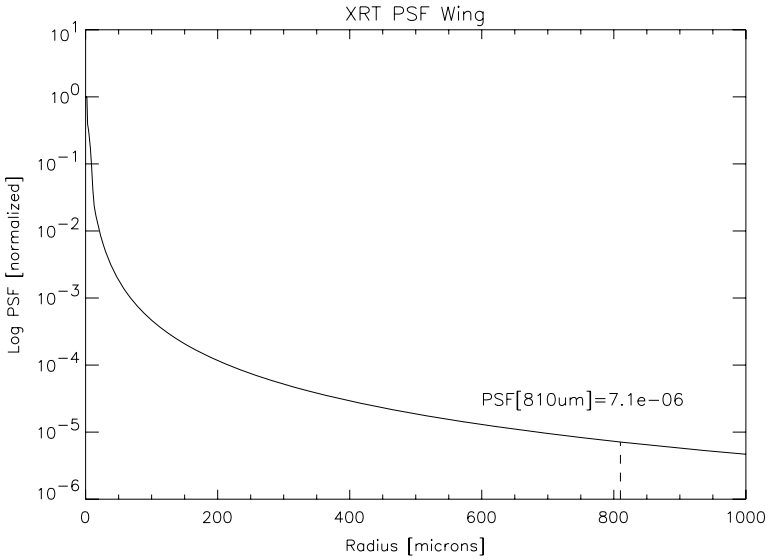

Figure 14 The wing response of the XRT PSF at a range of positions between 0 and 1000 μm from the core center. A 2D Lorentzian model was fit to this dataset; see text for details.

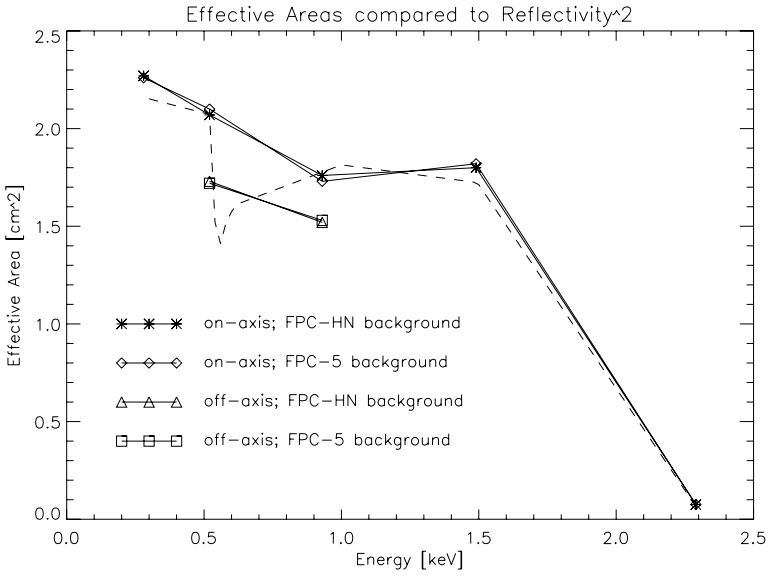

Figure 15 The effective area of the XRT optic as a function of energy, both on and off axis. The predicted on-axis areas for two reflections on the mirror (dashed line) are consistent with the on-axis measurements (asterisks and diamonds on solid lines). Off-axis measurements are also shown (triangles and squares on solid lines) for a field angle of 15.6 arcmin.

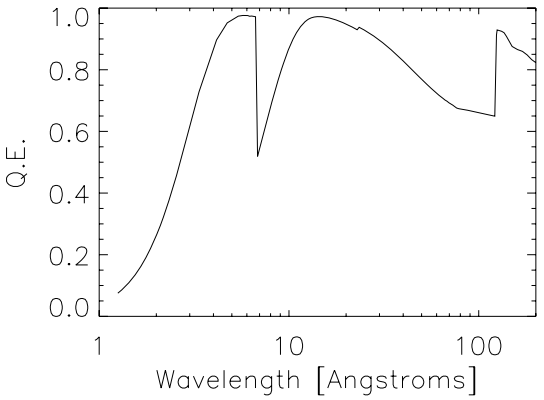

Figure 16 The nominal quantum efficiency curve for the XRT CCD camera, shown here for illustrative purposes only.

Table 7 Analysis filter measured (upper) vs. predicted (lower) transmissivities.

Emission line	C – K	O – K	Cu – L	Al – K	Mo – L
Energy (keV)	0.227	0.525	0.933	1.49	2.5
Filter	Measured transmission ± uncertainty Predicted transmission				
Al-mesh	23.8 ± 6.9	80.8 ± 8.5	93.7 ± 6.2	94.5 ± 5.2	77.4 ± 7.0
	21.2	72.1	91.9	97.6	92.0
Al-poly	24.0 ± 8.3	51.5 ± 8.6	77.4 ± 7.0	94.5 ± 5.2	89.6 ± 7.3
	19.4	50.3	82.0	94.6	91.2
C-poly	64.1 ± 5.5	7.9 ± 4.8	60.6 ± 4.8	79.2 ± 3.0	94.1 ± 7.0
	65.3	10.0	57.9	86.3	95.6
Ti-poly	41.8 ± 7.2	5.5 ± 3.2	33.9 ± 3.1	68.8 ± 4.4	91.0 ± 6.4
	34.0	3.1	33.0	71.7	89.3
Be-thin	5.6	–	26.1 ± 3.5	77.8 ± 5.6	90.7 ± 6.6
	0.0	0.1	27.8	72.6	91.1
Be-med	6.8	–	4.5 ± 2.7	48.9 ± 6.8	77.2 ± 5.3
	0.0	0.0	1.5	32.6	73.7
Al-med	–	–	2.3 ± 1.7	22.6 ± 4.4	2.5 ± 1.9
	0.0	0.0	0.6	23.6	0.2
Al-thick	–	–	–	5.1 ± 2.1	–
	0.0	0.0	0.0	6.0	0.0
Be-thick	–	–	–	–	7.8 ± 2.9
	0.0	0.0	0.0	0.0	6.7

5.2. Filter Transmission

As a check on the thickness of the analysis filters, their transmission at X-ray wavelengths was tested at the XACT facility in Palermo by using the same set of emission lines available for the XRCF testing; the energies associated with these emission lines were shown in Table 6.

The results of the measurements are shown in Table 7. The uncertainties in the measured transmissions are dominated by counting statistics. For some of the thick filters measured with the weaker emission lines, the time available for testing determined the number of photons that could be collected, so the error bars are relatively large. We see that, to within the measurement uncertainties, there is acceptable agreement in all cases between the predicted and the measured values.

5.2.1. CCD Quantum Efficiency

The calibration of the XRT camera is described in detail in a companion paper in this volume. For reference purposes we provide a calibration curve here, Figure 16, since this is part of the throughput calculation for the XRT instrument as a whole.

5.3. Total Telescope Throughput

The total throughput is the convolution of all relevant terms, including prefilter transmission, mirror effective area, analysis filter transmission, and CCD quantum efficiency. These contributions are summarized as an effective area, and the curves for all of the nine XRT filter channels are shown in Figure 17.

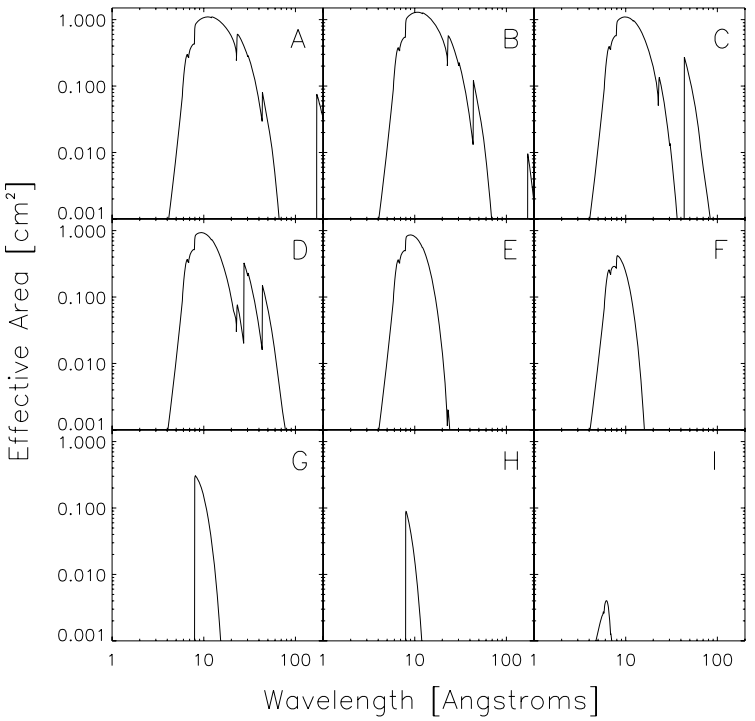

Figure 17 The total telescope throughput of the XRT for each of the nine X-ray filter channels. The labels indicate the filter channels as follows: A = Al-mesh, B = Al-poly, C = C-poly, D = Ti-poly, E = Be-thin, F = Be-med, G = Al-med, H = Al-thick, and I = Be-thick.

5.4. DEM Analysis

The next step after one is able to see the coronal structures is to determine their physical basic properties. Among these is the measurement of the amount of material present in the corona as a function of temperature, the differential emission measure, or DEM. The procedure we use for finding the best-fitting DEM for a given set of observations in several spectral channels has been described in Weber *et al.* (2005). We consider a set of images taken of an active region (AR) and we estimate the DEM in a given pixel. Our procedure then produces an iterative least-squares fit to the observations using a DEM represented by a spline with evenly spaced knots in $\log(T_e)$ space. With the forward modeling approach, we assume a differential emission measure and compare the predicted observations for each filter with the real observations, iterating the DEM until an acceptable fit is found.

The corona is known to be highly inhomogeneous in temperature, density, and magnetic field – the isothermal approximation is often inadequate for describing the optically thin solar atmosphere across length scales comparable to the span of an XRT pixel. The actual DEM distribution in an active region is thus expected to include material across a wide temperature range. We analyzed our DEM procedure using a realistic DEM model that is included in the CHIANTI database to evaluate the methods employed and to establish the number of observing channels needed to reproduce the input data. There is, in principle, no limit to the complexity of the model DEM that could be chosen. However, the physics of the situation – primarily the Boltzmann width of the spectral lines, causing them to be formed over a fairly wide temperature range in the corona – provides a fundamental limitation to the resolving power of any spectroscopic analysis (Craig and Brown, 1976). The amount of structure present in this model is reasonable for these tests.

Figure 18 suggests how well the input DEM can be reconstructed as a function of the number of observing channels used. In the left plot, four XRT channels have been used to perform fits. The figure shows the model AR DEM (solid line with two humps), the distribution of fitted DEMs (gray scale), and the median values of the 100 DEM runs (diamonds).

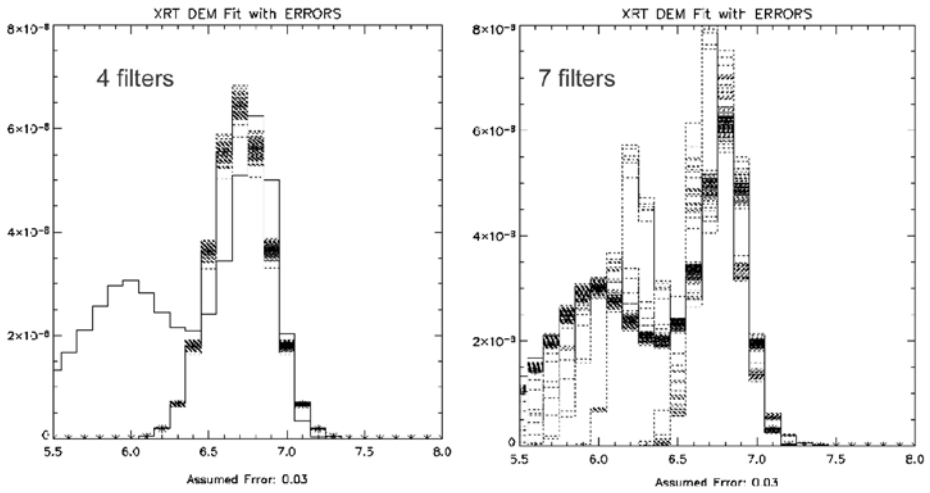

Figure 18 Two attempts at reconstructing an input model (solid histogram) of the DEM from a solar active region: (left) using four XRT channels produces a poor fit; (right) using seven channels yields an acceptable fit. Each panel shows 100 runs, with noise added for realism.

The DEM is fitted over the log temperature range 5.5 – 8.0 and 3% noise is assumed. These relatively high-T XRT filter channels determine the presence of the hotter peak of material, as indicated by the convergence of the median fit to the model DEM curve, but fail to detect the cooler material. The narrow uncertainty bands indicate that the fits are robust or, in the words of one author, "reliably bad."

In the right plot of Figure 18, the same model is fitted with seven channels; that is, we have included thinner filters in the analysis. It is obvious that the fitted DEMs more accurately reproduce the model DEM curve across the entire temperature range. Even though the uncertainty bands are not as constrained as in the left plot of Figure 18, they adequately indicate the presence and temperature of the cool component. To achieve good results in DEM reconstruction with XRT data, it is thus important to have observations in many (independent) channels.

5.4.0.1. The Number of Channels The physics of ionization fraction formation under coronal conditions combined with the range of temperatures found in the corona leads to a definite requirement on the number of independent channels that need to be recorded to reconstruct the emission measure distribution. The narrowness of the temperature range over which a typical ionization state is formed in the corona, combined with the requirement to have complete but nonredundant coverage, means that at least six channels must be used. This is shown explicitly in Figure 18, where we examine how the removal of even a single channel affects the quality of the DEM reconstruction for a typical active region.

DEM reconstruction thus requires observations in at least six independent channels, most of which should record a useful number of counts. This is the major reason for the choice of up to nine channels, spanning a large temperature range, in the XRT.

This analysis indicates that DEM determinations are data intensive, since they require that a large number of channels be used. Because telemetry is limited, as is onboard storage, and because some scientific objectives require high cadence (*i.e.*, the use of a single channel or a small number of channels), the multichannel DEM programs will need to be specifically scheduled when needed.

6. Conclusions

The X-ray telescope for *Hinode* is the highest resolution solar X-ray telescope ever flown (TRACE is EUV). The optical design and mirror quality ensure excellent imaging performance across the FOV and low scattering from bright flaring regions. In combination with the observations from the SOT and EIS, the XRT's broad temperature response, large dynamic range, and high throughput will achieve breakthrough science in the areas of CMEs (onset, coronal magnetic field structure, *etc.*), coronal heating (loop temperature dynamics, waves, and loop – loop interactions), flares, reconnection and jets (including the role of magnetic topology and energetics), and the relationship of the photospheric magnetic field evolution to coronal dynamics.

Acknowledgements We would like to thank Larry Hill and his staff at MSFC for effective and helpful management of this program and John Davis of MSFC for his experienced and useful advice and suggestions. We thank J. Pasachoff and the staff at Williams College for assistance with the VLI calibration. We also thank the staff at Goodrich (Danbury) for their effort and skill in fabricating the X-ray telescope and for permission to use the mirror performance figures.

References

Barbera, M., *et al*.: 2004, In: Hasinger, G., Turner, M.J.L. (eds.) *UV and Gamma-Ray Space Telescope Systems, Proc. SPIE* **5488**, 423.
Craig, I.J.D., Brown, J.C.: 1976, *Astron. Astrophys.* **49**, 239.
Deluca, E., *et al.*: 2005, *Adv. Space Res.* **36**, 1489.
Golub, L.: 2003, *Rev. Sci. Instrum.* **74**, 4583.
Kano, R., *et al*.: 2007, *Solar Phys.*, submitted.
Nariai, K.: 1987, *Appl. Opt.* **26**, 4428.
Nariai, K.: 1988, *Appl. Opt.* **27**, 345.
Smith, R.K., Brickhouse, N.S., Liedahl, D.A., Raymond, J.C.: 2001, *Astrophys. J.* **556**, L91.
Tsuneta, S., *et al.*: 1991, *Solar Phys.* **136**, 37.
Weber, M.A., Deluca, E.E., Golub, L., Sette, A.L.: 2005, In: Stepanov, A.V., Benevolenskaya, E.E., Kosovichev, A.G. (eds.) *Multi-Wavelength Investigations of Solar Activity, IAU Symp.* **223**, 321.
Werner, W.: 1977, *Appl. Opt.* **392**, 760.